

# Nematohydrodynamics for Colloidal Self-Assembly and Transport Phenomena

Sourav Mondal<sup>a</sup>, Apala Majumdar<sup>b</sup>, Ian M. Griffiths<sup>a,\*</sup>

<sup>a</sup>*Mathematical Institute, University of Oxford, Oxford OX2 6GG, UK*

<sup>b</sup>*Department of Mathematical Sciences, University of Bath, Bath BA2 7AY, UK*

---

## Abstract

### *Hypothesis*

Colloidal particles in a nematic liquid crystal (NLC) exhibit very different behaviour than that observed in an isotropic medium. Such differences arise principally due to the nematic-induced elastic stresses exerted as due to the interaction of NLC molecules with interfaces, which competes with traditional fluid viscous stresses on the particle.

### *Theory*

A systematic mathematical analysis of the behaviour of particles placed in the flow within an NLC microfluidic channel is performed using the continuum Beris–Edwards framework coupled to the Navier–Stokes equations. We impose strong homeotropic anchoring on the channel walls and weak homeotropic anchoring on the particle surfaces.

### *Findings*

The viscous and NLC forces act on an individual particle in opposing directions, resulting in a critical location in the channel where the particle experiences zero net force in the direction perpendicular to the flow. For multi-particle aggregation we show that the final arrangement is independent of the initial configuration, but the path towards achieving equilibrium is very different. The results of our work uncover new mechanisms for particle separation and routes towards self-assembly.

*Keywords:* nematic fluid, microchannel, Beris–Edwards, particle dynamics

---

## 1. Introduction

2 Nematic liquid crystals (NLCs) are important examples of complex anisotropic fluids  
3 with locally preferred directions [1]. NLCs combine the intrinsic fluidity of liquids with

---

\*Corresponding author

*Email address:* [ian.griffiths@maths.ox.ac.uk](mailto:ian.griffiths@maths.ox.ac.uk) (Ian M. Griffiths )

4 long-range orientational ordering of the constituent rod-like molecules. The orientational  
5 order couples with the flow and induces novel effects compared with isotropic Newtonian  
6 fluids, such as backflow, anisotropic stresses and multiple viscosities. The study of NLCs  
7 in microfluidic environments is relatively new, with substantial experimental interest since  
8 around 2011. Subsequently, experimentalists have highlighted the immense potential of  
9 NLC microfluidics for transport, mixing and particle separation [2, 3], while the ability of  
10 NLCs to spontaneously organize micron-size particles into regular patterns shows great  
11 promise [4]. For example, it is possible to generate defect or disclination lines in an  
12 NLC microfluidic set-up with an appropriate choice of boundary conditions, material  
13 parameters, temperature and flow effects and these defect lines can naturally attract  
14 colloidal particles or micro-cargo, which are subsequently transported along these lines  
15 as self-assembled chains [3, 5]. Further, the forces facilitating spatial-reorganization of  
16 colloidal dispersions in an NLC medium are two to three orders of magnitude higher than  
17 in water-based colloids [6, 7].

18 In the bulk NLC, additional long-range interactions between particles are present be-  
19 cause of the competition between elasticity and the interaction between NLC molecules  
20 and surfaces (termed ‘anchoring’), implying that colloids suspended in a nematic ma-  
21 trix are qualitatively different from their isotropic analogues. The particle sets a certain  
22 director distortion around itself, due to the surface anchoring conditions; the director  
23 distortions lead to long-range elastic interactions of the particle with the bounding walls  
24 (or neighbouring interfaces); and the nematic order leads to an anisotropy in the Stokes  
25 drag [8, 9]. These features mean that rich self-ordering phenomena can be observed,  
26 which is characterized by strong interplay between the colloidal size, NLC anisotropies,  
27 particle and surface anchoring properties [3, 10, 11, 12].

28 There is a wealth of literature on nematohydrodynamics in the absence of particle inclu-  
29 sions [13, 14]. The analysis of the impact of placing a particle in an NLC has generally  
30 been focused on how the NLC reorders around a single particle that is held in posi-  
31 tion [15] or the transitions in the flow profiles [16, 17]. More recent experimental studies  
32 have focused on the dynamic behaviour of (finite sized) suspended colloidal particles in  
33 a nematic-fluid flow [1, 3, 7, 18].

34 Our work is motivated by the experiments conducted by Sengupta et al. in [2]. Here  
35 the authors study an NLC microfluidic set-up experimentally and numerically in three

36 different flow regimes: weak, medium and strong, and report on both the flow profiles  
37 and the averaged local molecular alignment profiles, referred to as “director” profiles in  
38 the continuum-modelling literature. The surfaces of the microfluidic channel are treated  
39 to induce homeotropic boundary conditions, so that the nematic molecules are preferen-  
40 tially anchored along the normal to the boundary surfaces, or equivalently the continuum  
41 “director” is parallel to the normal to the channel walls. A flow is induced by applying a  
42 pressure gradient at the inlet and the observations seem to be invariant across the width  
43 of the cell.

44 In this paper we focus on three separate aspects: (i) a static particle at the centre with  
45 variable anchoring strength on its boundary, (ii) the forces experienced by a particle  
46 inclusion due to hydrodynamic effects, nematic stresses and attractive forces induced by  
47 the boundary conditions and (iii) the dynamics of two and three particles in an NLC  
48 microfluidic environment including the transient dynamics.

49 We mathematically model the NLC microfluidic environment using the nematodynamics  
50 formulation used in [19]. The state of nematic alignment is described by a two-dimensional  
51 (2D) Landau-de Gennes (LdG)  $\mathbf{Q}$ -tensor, which is a symmetric traceless two-by-two ma-  
52 trix with two degrees of freedom: an angle  $\theta$  that describes the preferred in-plane align-  
53 ment of the nematic molecules or the direction of the nematic director  $\mathbf{n}$ , and a scalar  
54 order parameter,  $s$ , that is a measure of the degree of alignment about the director  $\mathbf{n}$ .  
55 We investigate how the particles interact with the NLC environment in the absence and  
56 presence of flow, for both static and moving particles. The first example concerns a static  
57 particle in the NLC microfluidic cell with no fluid flow. For a given anchoring strength  
58 on the particle boundary, we study the director profile around the particle as a function  
59 of its size and, for a given particle size, we investigate the surrounding director profile as  
60 a function of anchoring strength. In both cases, there is a narrow window of parameters  
61 within which the director orientation on the particle boundary switches from uniform to  
62 normal/homeotropic and we numerically explore the switch in different cases. We then  
63 systematically study the force experienced by the particle including the effects of a flow  
64 field, particle surface anchoring, and the particle size. In particular, for a given anchor-  
65 ing strength and flow velocity, there is a critical particle size (relative to the channel  
66 dimensions) such that, in contrast to conventional liquids, the force attains a maximum,  
67 decreasing for larger particles owing to the attractive forces exerted by the boundaries.

68 We conclude by studying the motion of two and three colloidal particles in the microfluidic  
69 channel, including the transient re-alignment dynamics, how the particles get attracted  
70 to each other starting from different initial configurations and are transported through  
71 the channel as an agglomerate.

## 72 2. Theory

73 We consider a two-dimensional NLC microfluidic channel (parallel-plate geometry) as  
74 shown in Fig. 1. The nematic director  $\mathbf{n} = (\cos \theta, \sin \theta)$ , represents the locally preferred  
75 in-plane alignment of the NLC molecules relative to the horizontal axis. We consider a  
76 circular particle, whose boundary is parameterized by the angle  $\phi$  to the horizontal axis.  
77 We apply strong homeotropic anchoring conditions on the channel walls (modelled by  
78 Dirichlet conditions) while the anchoring conditions on the colloidal particle are varied  
79 from weak to strong in terms of an anchoring coefficient. Provided the channel dimension  
80 into the page ( $z$  direction) is large compared with the channel height (in the  $y$  direction,  
81 i.e.,  $2L_2$  in Fig. 1) then this two dimensional approximation is valid [20, 21]. We note  
82 that the three-dimensional analogue of this two-dimensional set-up would in principle  
83 correspond to cylindrical particles. However, similar methods can be applied to stud-  
84 ied to spherical colloidal particles in an NLC microfluidic channel, though this requires  
85 further study. When these dimensions are comparable then the problem is fully three  
86 dimensional, as seen in [22, 23]. Whilst we do not consider this scenario in this paper, we  
87 analyse this further in Appendix A of the Supplementary Information. The fluid flow in  
88 the device is driven by an external pressure difference and by the nematic ordering. We  
89 impose no-slip conditions on the channel walls and particle surface.

The flow hydrodynamics are described by the incompressible Navier–Stokes equations with an additional stress ( $\boldsymbol{\sigma}$ ) due to the NLC orientational ordering [19, 24],

$$\nabla \cdot \mathbf{u} = 0, \tag{1}$$

$$\rho \left( \frac{\partial \mathbf{u}}{\partial t} + \mathbf{u} \cdot \nabla \mathbf{u} \right) = -\nabla p + \nabla \cdot (\mu[\nabla \mathbf{u} + (\nabla \mathbf{u})'] + \boldsymbol{\sigma}). \tag{2}$$

Here  $\nabla = \left( \frac{\partial}{\partial x}, \frac{\partial}{\partial y} \right)$ ,  $\rho$  and  $\mu$  are the density and viscosity of the fluid medium respectively,  $p$  is the hydrodynamic pressure,  $\mathbf{u}$  is the fluid velocity and  $\mu[\nabla \mathbf{u} + (\nabla \mathbf{u})']$  is the viscous stress experienced by the fluid ( $[\nabla \mathbf{u}]'$  is the transpose of  $\nabla \mathbf{u}$ ). The NLC stress ( $\boldsymbol{\sigma}$ ) is



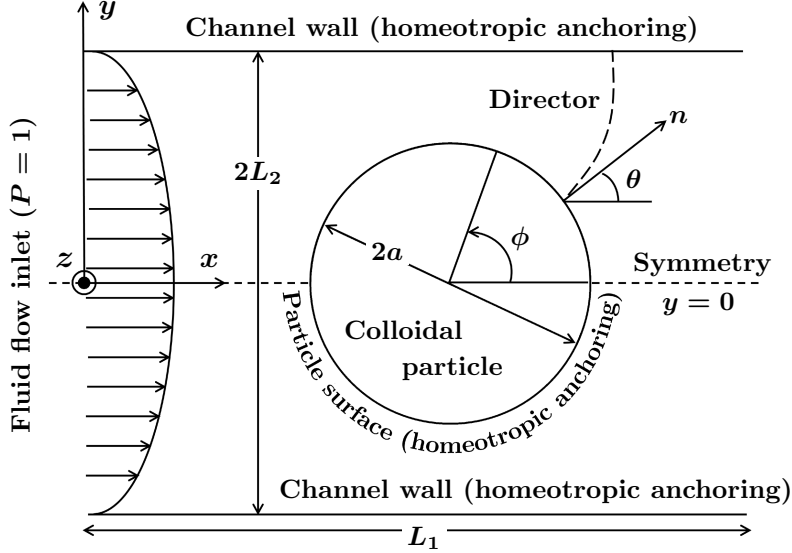


Figure 1: Schematic of the problem definition and system geometry showing the reference co-ordinate system. The fluid flow is in the direction of positive  $x$ .

given by [19, 13, 25, 26, 2],

$$\boldsymbol{\sigma} = -\lambda s \mathbf{h} + \mathbf{q} \mathbf{h} - \mathbf{h} \mathbf{q}, \quad (3)$$

where  $s = \sqrt{2}|\mathbf{q}|$  is the scalar order parameter and  $\mathbf{h}$  is the molecular field, which controls the relaxation to equilibrium and is given by

$$\mathbf{h} = \kappa \nabla^2 \mathbf{q} - A \mathbf{q} - C |\mathbf{q}|^2 \mathbf{q}. \quad (4)$$

Here,  $\mathbf{q}$  is the nematic order parameter, a symmetric and traceless  $2 \times 2$  matrix, used to describe the NLC state and is referred to as the two-dimensional LdG tensor [27],

$$\mathbf{q} = \begin{pmatrix} q_{11} & q_{12} \\ q_{12} & -q_{11} \end{pmatrix}; \quad (5)$$

90  $\kappa$  is the NLC elastic constant,  $A$  and  $C$  are material and temperature-dependent coefficients  
91 and  $\lambda$  is the (dimensionless) NLC alignment parameter, which reflects whether the  
92 NLC response is affected by the fluid strain or vorticity and is determined experimen-  
93 tally [25, 28, 29].

The tensor  $\mathbf{q}$  and the director  $\mathbf{n}$  are related by  $\mathbf{q} = s(\mathbf{n} \otimes \mathbf{n} - \mathbf{I}/2)$  where  $\mathbf{I}$  is the identity matrix in 2D and  $s^2 = 2|\mathbf{q}|^2$ . We recover the director angle from the relation  $\theta = \frac{1}{2} \tan^{-1}(q_{12}/q_{11})$ . In [19], the evolution equation for  $\mathbf{q}$  is given by [30, 19, 24]

$$\frac{\partial \mathbf{q}}{\partial t} + \mathbf{u} \cdot \nabla \mathbf{q} = \frac{1}{2} \lambda s [\nabla \mathbf{u} + (\nabla \mathbf{u})'] + \mathbf{q} \boldsymbol{\omega} - \boldsymbol{\omega} \mathbf{q} + \frac{1}{\Gamma} \mathbf{h}, \quad (6)$$

where  $\Gamma$  is the rotational diffusion coefficient [25] and  $\boldsymbol{\omega} = \nabla \times \mathbf{u}$  is the anti-symmetric part of the velocity gradient tensor, or vorticity tensor. We label  $\mathbf{q}$  as a 2D vector with two independent components,  $\mathbf{q} = (q_{11}, q_{12})$  where  $q_{11} = \frac{\varepsilon}{2} \cos 2\theta$  and  $q_{12} = \frac{\varepsilon}{2} \sin 2\theta$ . We impose strong homeotropic conditions on the channel walls so that

$$\mathbf{q} = \left( \frac{2|A|}{C} \right)^{1/2} \left( \boldsymbol{\nu}_{\pm} \otimes \boldsymbol{\nu}_{\pm} - \frac{\mathbf{I}}{2} \right), \quad (7)$$

94 where  $\boldsymbol{\nu}_{\pm} = (0, \pm 1)$  are the unit outward normals at the channel walls  $y = \pm L_2$ , where  
 95  $L_2$  is the channel half height as depicted in Fig. 1.

On the particle, we apply a mixed anchoring condition,

$$-\kappa \nabla q_{11} \cdot \boldsymbol{\nu}_p = w \left( q_{11} + \sqrt{\frac{A}{2C}} \right), \quad (8a)$$

$$-\kappa \nabla q_{12} \cdot \boldsymbol{\nu}_p = w q_{12}, \quad (8b)$$

96 where  $\boldsymbol{\nu}_p$  is the unit normal to the particle surface and  $w$  is an anchoring-strength pa-  
 97 rameter. When  $w = 0$ , (8) reduces to Neumann boundary conditions and  $w \rightarrow \infty$  is the  
 98 Dirichlet strong homeotropic anchoring limit.

### 99 2.1. Non-dimensionalization

We non-dimensionalize equations (1)–(6) by applying the following scalings:

$$\begin{aligned} X &= \frac{x}{L_2}, & Y &= \frac{y}{L_2}, & U &= \frac{u}{u_0}, \\ V &= \frac{v}{u_0}, & P &= \frac{pL_2}{\mu u_0}, & T &= \frac{u_0 t}{L_2}, \end{aligned} \quad (9)$$

where  $u_0$  is the mean channel velocity and  $\mu$  is the fluid viscosity. The dimensionless versions of Eqs. (1)–(4) are then

$$\frac{\partial U}{\partial X} + \frac{\partial V}{\partial Y} = 0, \quad (10)$$

$$\begin{aligned} Re \left( \frac{\partial U}{\partial T} + U \frac{\partial U}{\partial X} + V \frac{\partial U}{\partial Y} \right) &= -\frac{\partial P}{\partial X} + \frac{\partial^2 U}{\partial X^2} + \frac{\partial^2 U}{\partial Y^2} \\ &+ \frac{1}{Er} \frac{|A^*|}{2C^*} \frac{\partial}{\partial X} (-\lambda SH_{11}) + \frac{1}{Er} \frac{|A^*|}{2C^*} \frac{\partial}{\partial Y} (-\lambda SH_{12} - \eta), \end{aligned} \quad (11)$$

$$\begin{aligned} Re \left( \frac{\partial V}{\partial T} + U \frac{\partial V}{\partial X} + V \frac{\partial V}{\partial Y} \right) &= -\frac{\partial P}{\partial Y} + \frac{\partial^2 V}{\partial X^2} + \frac{\partial^2 V}{\partial Y^2} \\ &+ \frac{1}{Er} \frac{|A^*|}{2C^*} \frac{\partial}{\partial X} (-\lambda SH_{12} + \eta) + \frac{1}{Er} \frac{|A^*|}{2C^*} \frac{\partial}{\partial Y} (\lambda SH_{11}). \end{aligned} \quad (12)$$

Here  $\mathbf{H}$  is the dimensionless molecular field given by

$$\mathbf{H} = \frac{\partial^2 \mathbf{Q}}{\partial X^2} + \frac{\partial^2 \mathbf{Q}}{\partial Y^2} - A^* \left( 1 + \frac{1}{4} S^2 \right) \mathbf{Q}, \quad (13)$$

where

$$\begin{aligned} A^* &= \frac{AL_2^2}{\kappa}, & C^* &= \frac{CL_2^2}{\kappa}, & \mathbf{H} &= \mathbf{h} \frac{L_2^2}{\kappa} \sqrt{\frac{2C^*}{|A^*|}}, \\ \mathbf{Q} &= \mathbf{q} \sqrt{\frac{2C^*}{|A^*|}}, & \eta &= 2(Q_{12}H_{11} - Q_{11}H_{12}), & S &= s \sqrt{\frac{2C^*}{|A^*|}}; \end{aligned} \quad (14)$$

$Er = u_0 \mu L_2 / \kappa$  denotes the Ericksen number, the ratio of the viscous to NLC elastic forces and  $Re = \rho u_0 L_2 / \mu$  is the Reynolds number, which quantifies the relative magnitude of the inertial to viscous forces. In microfluidic flows,  $Re \ll 1$  (Table 1 gives typical operating regimes  $10^{-6} < Re < 10^{-3}$ ), which reduces Eqs. (11)–(12) to a Stokes flow (where the inertial terms on the left-hand side are ignored), so that

$$\frac{\partial P}{\partial X} = \frac{\partial^2 U}{\partial X^2} + \frac{\partial^2 U}{\partial Y^2} + \frac{1}{Er} \frac{|A^*|}{2C^*} \frac{\partial}{\partial X} (-\lambda S H_{11}) + \frac{1}{Er} \frac{|A^*|}{2C^*} \frac{\partial}{\partial Y} (-\lambda S H_{12} - \eta), \quad (15)$$

$$\frac{\partial P}{\partial Y} = \frac{\partial^2 V}{\partial X^2} + \frac{\partial^2 V}{\partial Y^2} + \frac{1}{Er} \frac{|A^*|}{2C^*} \frac{\partial}{\partial X} (-\lambda S H_{12} + \eta) + \frac{1}{Er} \frac{|A^*|}{2C^*} \frac{\partial}{\partial Y} (\lambda S H_{11}). \quad (16)$$

For the flow problem, we apply the following boundary conditions: no slip and no penetration on the channel walls and particle surface,

$$U = 0, \quad V = 0, \quad (17)$$

on  $Y = \pm 1 \forall X$  and  $X^2 + Y^2 = R^2$ , where  $R = r/L_2$  is the dimensionless radius of the colloidal particle and pressure boundary conditions at the channel entrance and exit,

$$P = 1 \quad \text{on } X = -L_1/2L_2, \quad -1 \leq Y \leq 1, \quad (18)$$

$$P = 0 \quad \text{on } X = L_1/2L_2, \quad -1 \leq Y \leq 1. \quad (19)$$

The dimensionless versions of the evolution equations (6) are

$$\frac{\partial Q_{11}}{\partial T} + U \frac{\partial Q_{11}}{\partial X} + V \frac{\partial Q_{11}}{\partial Y} = \lambda S \frac{\partial U}{\partial X} - Q_{12} \left( \frac{\partial V}{\partial X} - \frac{\partial U}{\partial Y} \right) + \frac{\mu/\Gamma}{Er} H_{11}, \quad (20)$$

$$\frac{\partial Q_{12}}{\partial T} + U \frac{\partial Q_{12}}{\partial X} + V \frac{\partial Q_{12}}{\partial Y} = \frac{1}{2} \lambda S \left( \frac{\partial V}{\partial X} + \frac{\partial U}{\partial Y} \right) - Q_{11} \left( \frac{\partial V}{\partial X} - \frac{\partial U}{\partial Y} \right) + \frac{\mu/\Gamma}{Er} H_{12}. \quad (21)$$

The strong homeotropic boundary conditions (7) translate to

$$Q_{11} = -1, \quad Q_{12} = 0. \quad (22a,b)$$

The anchoring conditions on the particle, (8), become

$$-\tilde{\nabla}Q_{11} \cdot \boldsymbol{\nu}_p = W(Q_{11} + 1), \quad (23a)$$

$$-\tilde{\nabla}Q_{12} \cdot \boldsymbol{\nu}_p = WQ_{12}, \quad (23b)$$

100 where  $\tilde{\nabla} = (\partial/\partial X, \partial/\partial Y)$  is the dimensionless gradient operator, and  $W = wL_2/\kappa$  is the  
101 dimensionless anchoring parameter.

## 102 2.2. Force exerted on the particle

The total dimensional force (per unit length),  $\mathbf{f}$ , on a particle of radius  $r$  in an NLC medium [31, 32, 33] is given by,

$$\mathbf{f} = \int_{\psi} (-p\mathbf{I} + \mu[\nabla\mathbf{u} + (\nabla\mathbf{u})'] + \boldsymbol{\sigma}) \cdot \boldsymbol{\nu}_p d\xi, \quad (24)$$

where  $\psi$  defines the circular boundary of the particle and  $\boldsymbol{\nu}_p$  denotes the unit normal to the surface. The displacement of the particle can be calculated from the Stokes drag equation

$$\mathbf{f} = 3\pi\mu(\mathbf{u} - \dot{\mathbf{x}}_p), \quad (25)$$

103 where  $\mathbf{x}_p = (x_p, y_p)$  denotes the instantaneous position of the particle centre and a dot  
104 represents differentiation with respect to time.

Non-dimensionalizing Eq. (24) via (9) and choosing the natural force scaling  $\mathbf{F} = \mathbf{f}/\mu u_0$  gives the dimensionless drag ( $F_x$ ) and lift ( $F_y$ ) components of the force experienced by the particle (i.e., the forces in the  $x$  and  $y$  directions, respectively),

$$F_x = \int_{\Psi} \left[ \left( 2\frac{\partial U}{\partial X} - P - \frac{1}{Er} \frac{|A^*|}{2C^*} \lambda SH_{11} \right) \nu_x + \left( \frac{\partial U}{\partial Y} + \frac{\partial V}{\partial X} - \frac{1}{Er} \frac{|A^*|}{2C^*} (\lambda SH_{12} + \eta) \right) \nu_y \right] d\Omega, \quad (26)$$

$$F_y = \int_{\Psi} \left[ \left( \frac{\partial U}{\partial Y} + \frac{\partial V}{\partial X} - \frac{1}{Er} \frac{|A^*|}{2C^*} (\lambda SH_{12} - \eta) \right) \nu_x + \left( 2\frac{\partial V}{\partial Y} - P + \frac{1}{Er} \frac{|A^*|}{2C^*} \lambda SH_{11} \right) \nu_y \right] d\Omega, \quad (27)$$

where  $\Psi$  denotes the perimeter of the particle in the dimensionless domain and  $\boldsymbol{\nu}_p = (\nu_x, \nu_y)$ . The dimensionless version of Eq. (25) reads as

$$3\pi(U - \dot{X}_P) = F_x, \quad (28a)$$

$$3\pi(V - \dot{Y}_P) = F_y, \quad (28b)$$

105 where  $\dot{X}_P = dX_P/dT$  and  $\dot{Y}_P = dY_P/dT$  are the respective dimensionless particle velocity  
 106 components.

Table 1: Typical values of the physical parameters

Parameter [units]	Typical values [reference]
Elastic constant, $\kappa$ [ $pN$ ]	40 [2]
Length of the microchannel, $L_1$ [ $\mu m$ ]	50
Half-height of the microchannel, $L_2$ [ $\mu m$ ]	10
Particle radius, $r$ [ $\mu m$ ]	3
Mean fluid velocity, $u_0$ [ $\mu m/s$ ]	10
Rotational diffusion constant, $\Gamma$ [ $Pa s$ ]	7.3 [2]
Viscosity, $\mu$ [ $Pa s$ ]	0.01 [21]
NLC material property, $A$ [ $MJ/m^3$ ]	-0.172 [2]
NLC material property, $C$ [ $MJ/m^3$ ]	1.72 [2]
Dimensionless parameters used in calculation	
NLC alignment parameter, $\lambda$	1 [2]
Dimensionless particle radius, $R$	0.3
Reynolds number, $Re$	0.0001
Ericksen number, $Er$	0.01 – 100
Parameter, $ A^* /C^*$	0.1
Relative anchoring strength, $\log W$	3

### 107 3. Results and Discussion

108 The coupled system of the equations (10–23) are solved numerically using a finite element  
 109 software COMSOL v5.2 [34]. The details of the numerical techniques and the solver  
 110 settings are given in the Supplementary Information (Section B).

### 111 3.1. Static particle and no fluid flow

112 We first compute the equilibrium director profiles and the order parameter  $S$  in the  
113 absence of a flow field  $U = V = 0$  (or  $Er = 0$ ). In this case we need only solve Eqs. (20)  
114 and (21), which reduce to  $H_{11} = H_{12} = 0$  respectively, subject to the boundary conditions  
115 (22) and (23). We vary the anchoring strength parameter at the particle surface from  
116 weak to strong (homeotropic) anchoring (Fig. 2). There have been both experimental [35]  
117 and theoretical studies [36] where such ranges (over orders of magnitude) of the anchoring  
118 strength have been studied for physically realistic scenarios.

119 In [35] there are several surface anchoring values reported for different combinations of  
120 NLC materials and surfaces, which correspond to  $\log W \approx 0 - 2$ . In [36] the authors  
121 have studied the effect of surface anchoring strength (varying from  $\log W \approx 1 - 2$ ) on the  
122 stability of the nematic ordering.

123 Surface anchoring strengths can be altered by photo-excitation [37], electric or magnetic  
124 fields [38, 39] or chemical surface functionalization [40]. Defects along the axial symmetry  
125 line ( $Y = 0$ ) are observed, consistent with the literature reports [14, 41, 17, 42]. The  
126 contours of the order parameter are also qualitatively similar to the report of Fukuda  
127 et al. [13] and Sengupta et al. [43]. For low anchoring strengths, the defects are almost  
128 pinned to the particle surface, migrating away from the particle surface with increasing  
129 anchoring strength; at present there has been little experimental investigation along these  
130 lines.

131 The director field on the particle surface is very sensitive to the change in anchoring  
132 strength in the range  $0.5 < \log W < 1$  for  $R = 0.3$  (Fig. 3a). The anchoring switches  
133 from being effectively uniform (zero anchoring) to homeotropic (strong anchoring) within  
134 this range.

135 The effect of the particle size has a profound influence on the director field (Fig. 3b–  
136 d), particularly with increasing anchoring strength. As the particle size increases, the  
137 distance between the particle surface and channel walls reduces, inducing strong coupling  
138 between the directors on the particle surface and on the channel walls. Again there  
139 is a narrow range of  $R$  over which the director orientation switches from uniform to  
140 homeotropic on the particle boundary. The values of  $R$  in the transition region decrease  
141 with increasing  $\log W$  (Fig. 3b–d). For example, in the case of  $W = 3.2$  the transition  
142 occurs for  $0.7 < R < 0.8$  (Fig. 3c), whereas for  $W = 10$ , the same occurs in the range

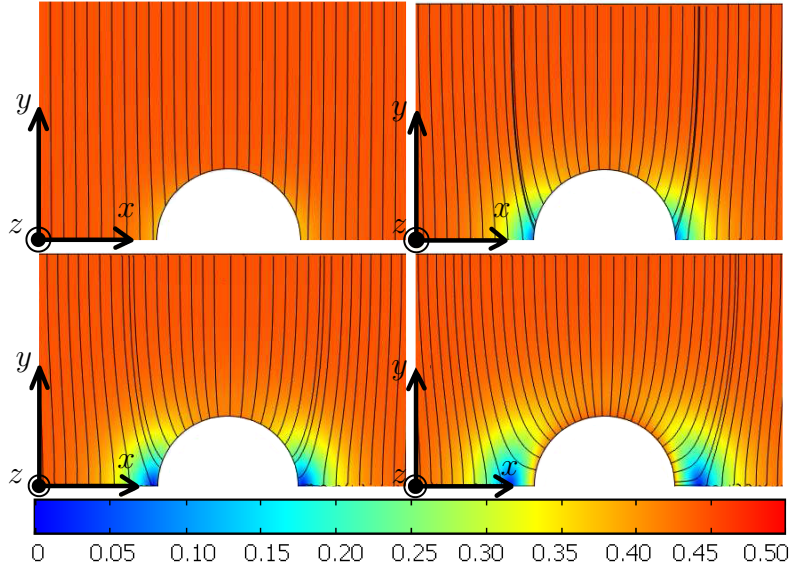


Figure 2: Orientation of the director field around the particle with homeotropic boundary conditions on the channel walls with zero flow field ( $Er = 0$ ) for  $R = 0.3$ . The angle of the director orientation,  $\theta$  (quiver angle) is given by  $\theta = \frac{1}{2} \tan^{-1}(Q_{12}/Q_{11})$ . The anchoring strength on the particle surface is varied from weak to strong. (a)  $\log W = 0$ , (b)  $\log W = 0.8$ , (c)  $\log W = 1$  and (d)  $\log W = 2$ . The solid lines represent the director profiles ( $\theta$ ) and the background contour represent the magnitude of the order parameter  $S$ . Due to symmetry we show only half of the channel. The values of the relevant parameters used for the calculation are given in Table 1.

143  $0.1 < R < 0.3$  (Fig. 3d).

### 144 3.2. Static particle with fluid flow effects

145 Next, we include a flow field but hold the particle in place. We solve Eqs. (15), (16), (20),  
 146 (21) subject to Eqs. (17)–(19), (22), (23) for the steady-state situation and  $\partial \mathbf{Q} / \partial T = 0$   
 147 in Eqs. (20) and (21). This models a system with an obstacle (for example, a static  
 148 micropillar [18]). On increasing the Ericksen number (while maintaining  $Re \ll 1$ ) we  
 149 observe three distinct regimes: weak, moderate and strong. The weak regime occurs  
 150 for small  $Er$ . Here, the director profiles remain almost unchanged compared with those  
 151 observed in the previous section with no flow field while the flow profile is significantly  
 152 different to classical Poiseuille flow (Fig. 4a).

153 There are two stable director profiles, known as the horizontal (H) and vertical (V) states  
 154 (Fig. 4d). The H and V states have different orientations at the channel centre (H-state,  
 155  $\theta = 2n\pi$  and in V-state,  $\theta = (n + 0.5)\pi$  where  $n = 0, 1, 2, 3, \dots$ ). In the H-state the  
 156 directors splay, whereas in the V-state the director has a bent profile [44]. As the flow  
 157 field is increased (through increasing  $Er$ ) we enter the moderate flow regime (Fig. 4b),

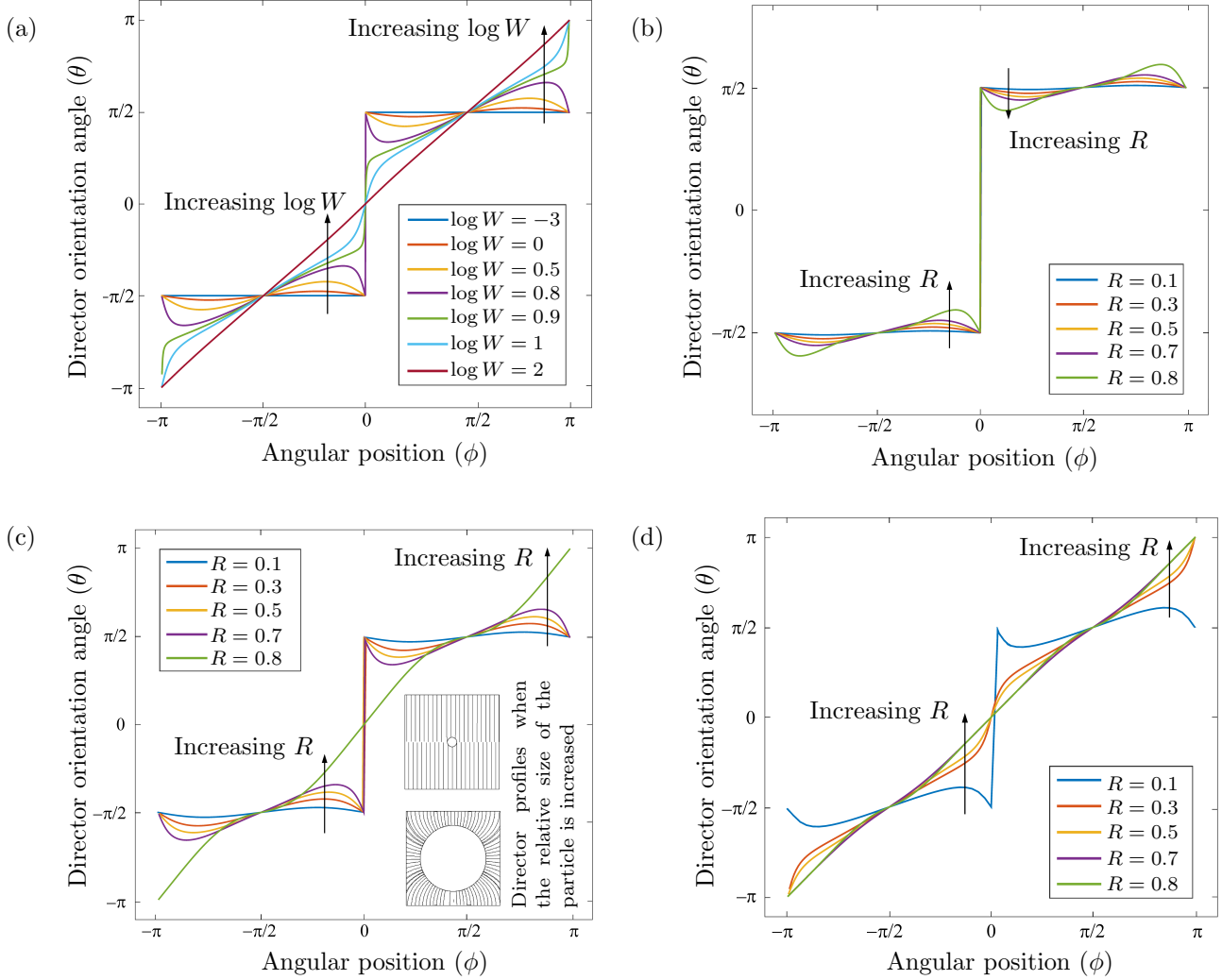


Figure 3: Variation of the director angle on the particle surface, with zero flow field ( $Er = 0$ ) with different particle sizes and anchoring strength. In (a) the anchoring strength is increased with  $\log W = -3, 0, 0.5, 0.8, 0.9, 1$  and  $2$  (in the direction of the arrow), for  $R = 0.3$ . In (b-d) the particle size is increased as  $R = 0.1, 0.3, 0.5, 0.7$  and  $0.8$  (in the direction of the arrow) for (b)  $\log W = 0$ , (c)  $\log W = 0.5$  (inset: qualitative visualization of the director orientation corresponding to  $R = 0.1$  and  $0.8$ ), and (d)  $\log W = 1$ . Note that the particle is located at the centre of the channel with homeotropic boundary conditions on the surface. The values taken for all other parameters used for the calculation are given in Table 1.



158 one primarily observes the V-state and the flow begins to assume a parabolic profile  
159 (Fig. 4b).

160 As we further increase the flow rate (i.e., increase  $Er$ ), the NLC stress weakens and we  
161 enter the strong regime (see Eqs. 15 and 16). The director field adapts to the more  
162 energetically favourable H-state configuration (Fig. 4c,d) and the flow assumes a fully  
163 developed Poiseuille profile. (Fig. 4c) [16]. This is consistent with the experimental  
164 observations of Sengupta et al. [2].

165 In Fig. 4e, we compare the location of the hyperbolic hedgehog defect on the leading  
166 side, as obtained from our numerical simulations, with the experimental results [18] for a  
167 channel with large aspect ratio, rendering the wall effect insignificant in the  $z$ -direction,  
168 consistent with our 2D set-up. We can see that the theoretical and experimental results  
169 are in close agreement for  $Er < 100$ . We also observe defects close to the particle body  
170 in the range  $\pi/2 \leq \phi \leq \pi$ , for moderate  $Er$  in agreement with the experiments in [13].  
171 Further, the distance of the defect on the trailing side from the particle surface is roughly  
172 0.17 times the diameter, in line with experiments that report this to be in the range of  
173 0.05–0.25 times the diameter [13].

174 Of principal interest is the force experienced by a particle as a result of the viscous and  
175 elastic stresses exerted on the particle surface, given by Eq. (24), since this ultimately  
176 dictates the motion of the particle. Since the particle is placed at the channel centre, the  
177 overall lift force ( $F_y$ ) is zero due to symmetry and the only force is in the  $x$  direction,  
178  $F_x$  (drag). As we increase  $Er$ , the force on the particle increases, in the direction of the  
179 hydrodynamic pressure gradient (Fig. 5a).

180 When the anchoring strength ( $\log W$  in Eq. 23) is increased, the driving force increases  
181 (Fig. 5b). This suggests that tuning the particle surface anchoring conditions by external  
182 stimuli, such as by photo-excitation [37] or an electric field [38] could assist in spatial  
183 reorganization in the nematohydrodynamic field.

184 While the viscous force on a particle due to hydrodynamic flow increases proportionally  
185 with particle radius [45], the effect of attractive normal boundary conditions on the  
186 channel walls is also felt as the particle size increases. These two forces act in competition,  
187 with the viscous forces attracting the particle to the centre and the wall forces drawing  
188 the particle towards the walls. As a result, a critical particle size exists for which the drag  
189 force is maximum ( $R \approx 0.56$  for the parameters considered in Fig. 5c). For an isotropic

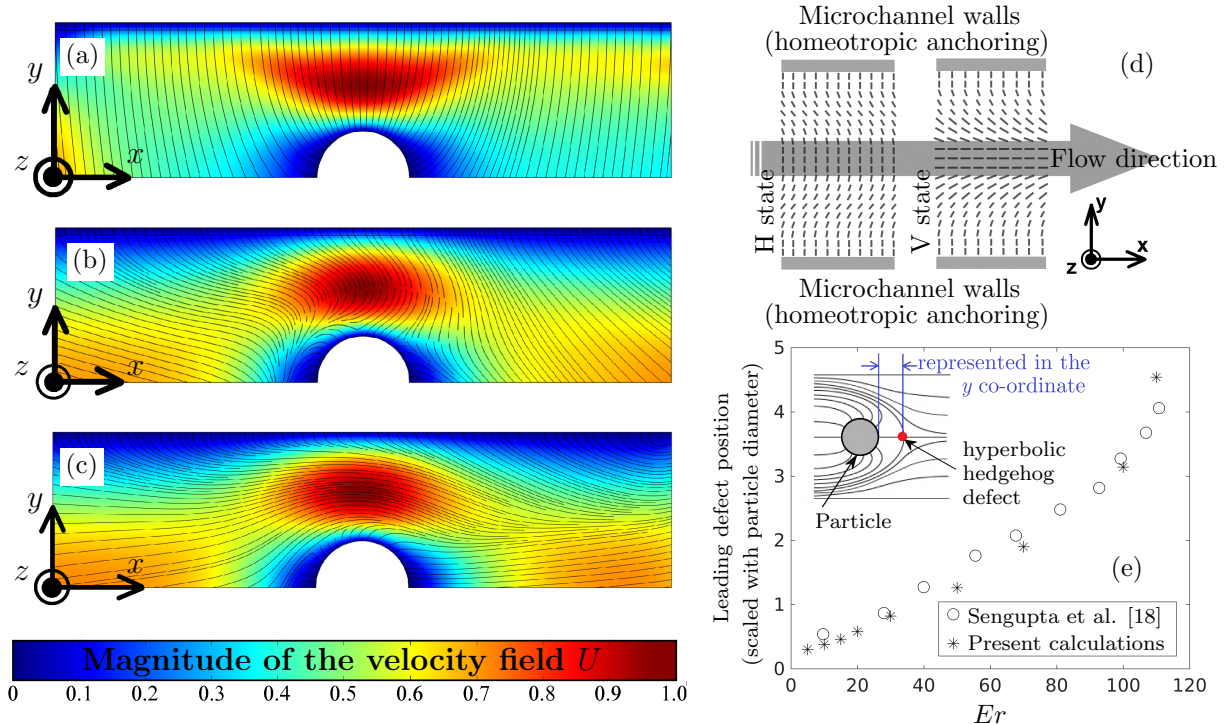


Figure 4: Profiles of the director orientation for (a)  $Er = 0.001$  (weak flow), (b)  $Er = 0.1$  (intermediate flow), (c)  $Er = 10$  (strong flow). The solid black lines show the director orientation in the channel. The fluid flow is in the positive  $x$  direction. Due to symmetry we show only half of the channel. The background colour contour represents the axial velocity field  $U$ . Here  $R = 0.3$ . The bottom edge of the domain ( $Y = 0$ ) is the symmetry condition. Homeotropic anchoring conditions are maintained on the channel walls as well as on the particle surface ( $W \rightarrow \infty$ ). The values taken for all other parameters used for the calculation are given in Table 1. (d) Schematic representation of the V and H state configurations of the director alignment [16]. In (e) we show the location of the leading hyperbolic hedgehog defect comparing the experimental observations [18] for a flow past a static micropillar (for large aspect ratio, justifying the 2D setup) with the present calculations. The values used in this calculation are corresponding to the experimental conditions [18].

190 Newtonian fluid, the drag force continues to increase with particle size, purely due to  
 191 the viscous stresses. On the other hand, the drag force in the NLC medium is sensitive  
 192 to the value of  $Er$ , the particle size and  $\log W$ .

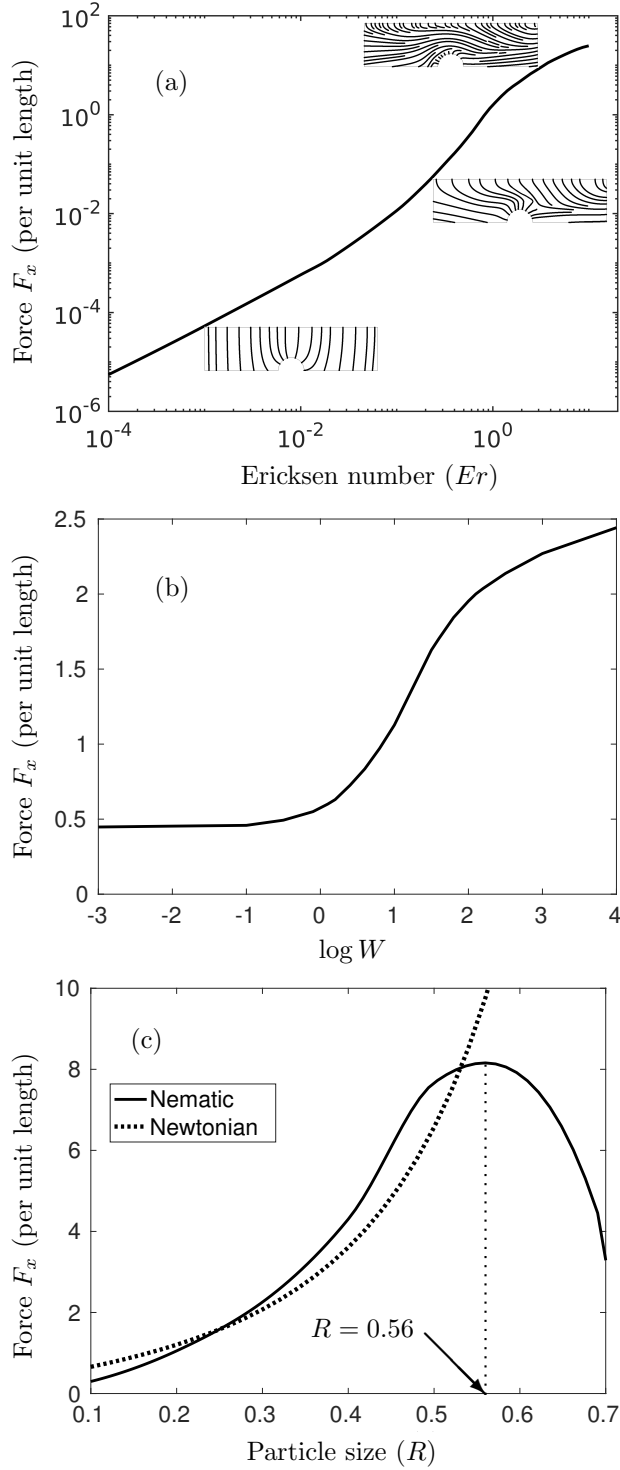


Figure 5: The axial force  $F_x$  on a static particle as a function of the (a) Ericksen number ( $Er$ ) (the snapshot of the director orientation in the channel at different  $Er = 0.001, 0.1, 10$  is shown as insets); (b) particle surface anchoring strength ( $\log W$ ); and (c) particle size ( $R$ ). The dotted line in (c) shows the force for an isotropic Newtonian fluid. The reference values of the parameters are  $R = 0.3$ ,  $Er = 1$  and  $\log W = 3$ . The values for all other parameters used for the calculation are given in Table 1.

### 193 3.3. Particle dynamics with fluid flow

#### 194 3.3.1. Single particle

195 Having characterized the effect of placing a static particle in an NLC we now study the  
196 director profiles and particle trajectories when we allow the particle to move in response  
197 to the nematohydrodynamic field. We fix the Ericksen number ( $Er = 0.02$ ) where the  
198 NLC elastic forces dominate over viscous forces [15, 13, 43] and solve the transient set  
199 of Eqs. (20)–(23) together with the flow hydrodynamics in Eqs. (10), (15)–(19). The  
200 particles are initially stationary ( $\dot{X}_P = \dot{Y}_P = 0$ ) and released into the flow, and the initial  
201 condition for the NLC and the fluid flow is the equilibrium configuration for fixed particle  
202 position (as found in Section 3.2). We impose strong anchoring conditions on the particle  
203 surface. To compare this situation with a Newtonian fluid, we simply set the elastic  
204 constant,  $\kappa = 0$  (thereby  $Er \rightarrow \infty$ ).

205 For the Newtonian case, the cross-plane position  $Y = 0$  is a stable equilibrium: if we  
206 release a particle from  $Y \neq 0$  then the particle will evolve towards the centre as a result  
207 of the viscous stress exerted on the particle [46]. This behaviour is also observed for the  
208 values of the NLC parameters considered here, with the relaxation time approximately  
209 following an exponential decay to  $Y = 0$  (Fig. 6a). As found in the previous section,  
210 the particle experiences two opposing forces: a viscous force, which acts to restore the  
211 particle towards the centre [46] and an attractive force between the strongly anchored  
212 channel wall and the particle surface [47], the latter of which is not present in a Newtonian  
213 fluid. The attractive force opposes the particle motion towards the centre, reducing the  
214 cross-stream velocity and increasing the time taken to reach the centre, compared with  
215 a Newtonian flow field (Fig. 6a,b).

216 Since there exists a competition between the NLC elastic stresses and the viscous forces  
217 on the colloidal particle, we hypothesize that there may be a critical vertical position  
218 for which the particle might migrate towards the wall instead of the centre. We analyse  
219 the lift force  $F_Y$  on the particle at  $T = 0$  to determine whether it migrates towards the  
220 centre ( $F_Y < 0$  since the particle is located at  $Y > 0$  initially) or the wall ( $F_Y > 0$ ).  
221 An unstable equilibrium is indeed found, at a critical vertical position,  $Y_P^*$ , for which the  
222 total lift force is zero (Fig. 6c). With increasing  $Er$ , the lift force approaches the limit of  
223 the Newtonian flow, where the particle always migrates towards the centre irrespective  
224 of its position. This suggests that, with a uniform particle distribution in the channel,

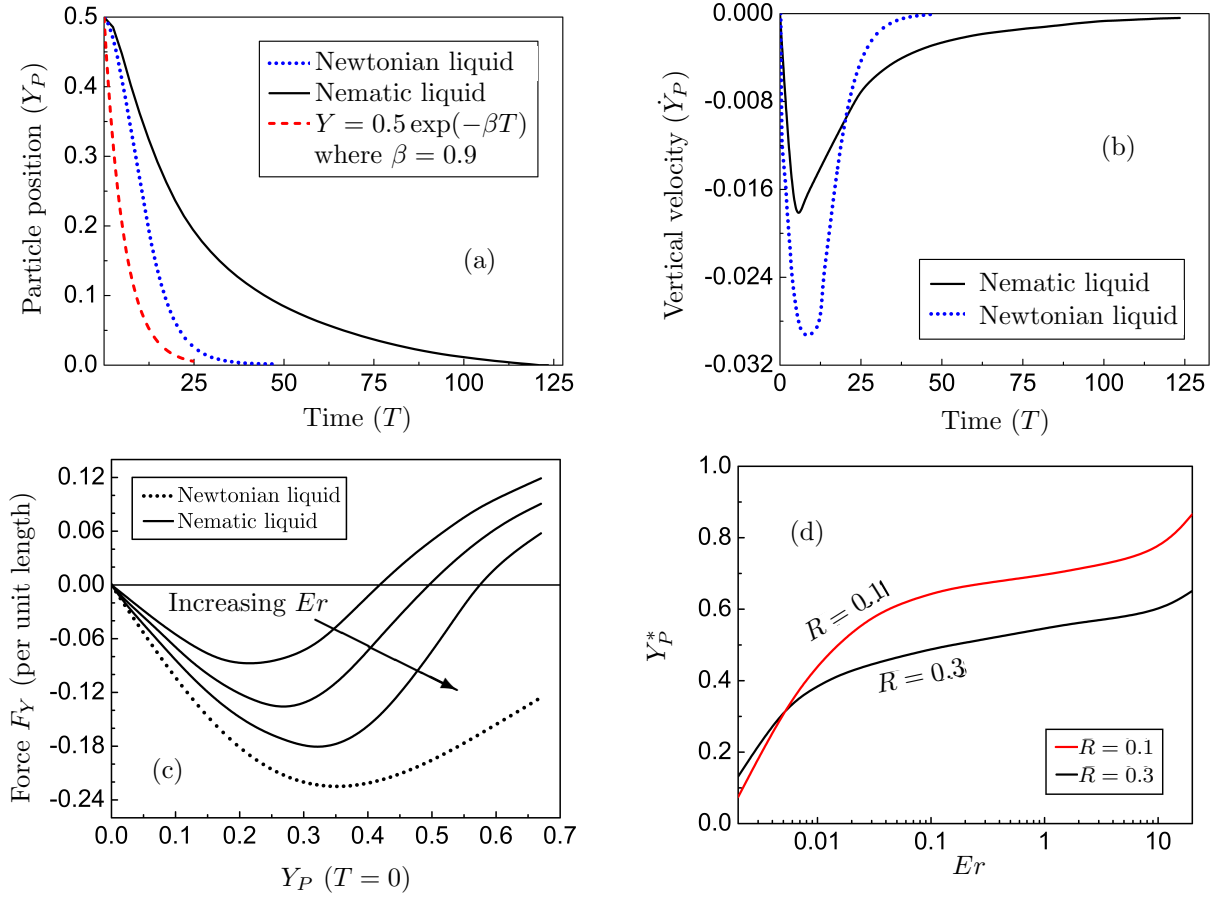


Figure 6: (a–b) Time evolution of a particle (black lines) that begins at position  $Y = 0.5$  as it relaxes towards the centre  $Y = 0$  in an NLC: (a) vertical coordinate of particle centre and (b)  $Y$ -component of the particle velocity. Here  $R = 0.3$  and  $Er = 0.02$ . (c) The lift force ( $F_Y$ ) experienced by the particle at different initial  $Y$  locations (of the particle centre) in the top half of the channel ( $Y > 0$ ), for  $R = 0.3$ . The three solid curves are for nematic liquid with  $Er = 0.02, 0.2$  and  $2$ . The anchoring conditions on the particle and channel walls are homeotropic. If  $F_Y < 0$  the particle migrates towards the centre. The dotted line is the behaviour of the particle in a viscous Newtonian flow, obtained by setting the elastic constant,  $\kappa = 0$  leading to  $Er \rightarrow \infty$ . In the case of the Newtonian liquid the particle migrates towards the centre independent of its size [46]. (d) Variation of the critical  $Y$  position of the particle,  $Y_P^*$  (at  $T = 0$  for which  $F_Y = 0$ ) as a function of the Ericksen number for two different particle sizes. The values taken for all other parameters used for the calculation are given in Table 1. The anchoring conditions on the particle surface and channel walls are homeotropic.

225 particles located on either side of the critical  $Y_P$  separate out, moving either towards  
 226 the wall or towards the centre. This is somewhat similar to a Newtonian flow through a  
 227 channel with porous walls, where the particles tend to flow towards the wall due to the  
 228 transverse velocity induced by the suction (difference in pressure across the porous wall).  
 229 However, all particles eventually deposit on (or penetrate) the wall in this case, while

230 for an NLC medium, a fraction of the introduced particles attach to the wall while the  
231 remainder move to the channel centre. The critical  $Y$  location is dependent on the size of  
232 the particle, anchoring strength and Ericksen number (Fig. 6d). With increasing particle  
233 size, the director interaction is stronger, yielding smaller values of  $Y_P^*$ , as observed from  
234 Fig. 6d.

235 *3.3.2. Dual particle system*

236 When two particles are released side by side (with zero initial velocities  $\dot{X}_P = \dot{Y}_P = 0$   
 237 starting from  $X = 0, Y = \pm 0.5$ ) within the microchannel, the attractive NLC forces  
 238 between two homeotropically anchored particle surfaces results in significantly increased  
 239 velocities in the  $Y$  direction, with the particles eventually touching one another (Fig. 7  
 240 and Fig. S2 in the Supplementary Information). The time evolution of the separation  
 241 distance (see Fig. S2a in the Supplementary Information) is qualitatively similar to the  
 242 experimental observations in [10] for the case of the dominant elastic interactions ( $Er \ll$   
 243 1). Upon agglomeration, the overall drag force is adjusted according to Fig. 5c. There  
 244 are two stages in the dynamics: the first stage corresponds to the two isolated particles  
 245 attracting each other and moving towards each other in a straight line ( $T \lesssim 0.35$ ). In  
 246 the second stage, the agglomerate reorients due to the quadrupolar interactions ( $0.35 \lesssim$   
 247  $T \lesssim 1.1$ ) (Fig. S2) [9, 3]. Due to the quadrupolar interactions [9, 3], the particles reorient  
 248 themselves with the angle of inclination  $\theta_p \approx 39^\circ$ , with respect to the horizontal axis  $Y = 0$   
 249 measured in the anti-clockwise direction. This is corroborated by Mondiot et al. [48]  
 250 who find an angle of inclination  $\theta_p = \sqrt{\arccos(4/7)} \approx 40.9^\circ$ , obtained by minimizing the  
 251 quadrupolar interaction energy. This dual particle reorientation is driven by the minimum  
 252 energy configuration state as described in [49]. The experimental observations in the  
 253 literature support the attractive force in the direction of the quadrupolar interactions  
 254 [47, 50, 51, 52]. The calculation of the Landau-de Gennes free energy of the two isolated  
 255 particles suggests that the minimum energy depends on  $\theta_p$  and the separation distance  
 256 [47].

257 *3.3.3. Triple-particle system*

258 Finally, we consider the nematohydrodynamic effects on the mechanics of a triple-particle  
 259 system in an NLC medium, for particle radii  $R = 0.2$  (Fig. 8). In the first example,  
 260 one particle is placed at the centre  $X = Y = 0$  while the other two particles are at  
 261  $X = -2, Y = \pm 0.5$ . Initially all the particles are stationary ( $\dot{X}_P = \dot{Y}_P = 0$  at  $T = 0$ ).  
 262 For  $T \lesssim 0.1$  the two particles with initial position at  $X = -2, Y = \pm 0.5$ , aggregate before  
 263 approaching the third (central) particle (Fig. 8a-c). When the two-particle agglomerate  
 264 catches up with the single particle, the particles align themselves as an equiangular sys-  
 265 tem (the centres form an equilateral triangle) to minimize the overall energy, due to the  
 266 quadrupolar interactions (Fig. 8d). This is in close agreement with the experimental ob-

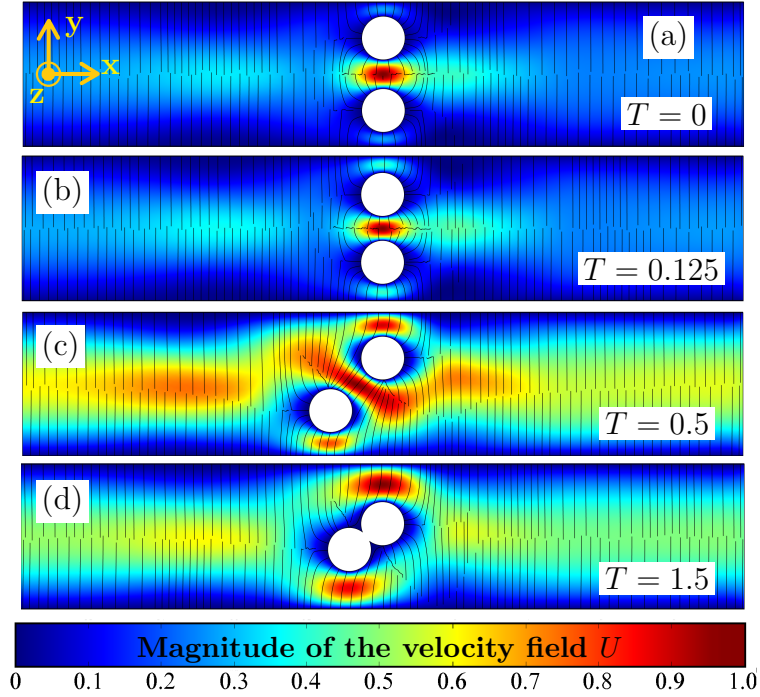


Figure 7: Snapshots showing the evolution with time of two particles placed in a microchannel located at  $X = 0, Y = \pm 0.5$ , as they approach each another and agglomerate: (a)  $T = 0$ ; (b)  $T = 0.125$ ; (c)  $T = 0.5$ ; and (d)  $T = 1.5$  (at which point the particles have reached their equilibrium configuration). Here  $R = 0.3$  and  $Er = 0.02$ . The anchoring conditions on the particle and channel walls are homeotropic. The values taken for all other parameters used for the calculation are given in Table 1. The boundary conditions on the particle surfaces and channel walls are homeotropic. The fluid flow is in the positive  $x$  direction. The background colour contour represents the magnitude of the axial velocity field  $U$ .

267 observations for colloidal assemblies in a 2D NLC system, where the interparticle orientation  
 268 angle in a triplet aggregate is found to be  $56 \pm 1^\circ$  [7].

269 There are three distinct velocity zones in Fig. 8:

270 (i) For  $T \lesssim 0.16$ , the two off-centred particles approach one another while accelerating  
 271 towards the third, central, particle. After these two particles aggregate, the overall drag  
 272 in the  $X$  direction increases (as predicted by Fig. 5c), since the cumulative size of the  
 273 dual-particle agglomerate is less than the critical size in Fig. 5c. The isolated central  
 274 third particle is largely unaffected by the two particles during this part of the motion.

275 (ii) For  $0.16 \lesssim T \lesssim 0.375$ , the agglomerate approaches the isolated particle at a higher  
 276  $X$ -velocity than the central particle. Since the timescale of the final re-orientation of  
 277 the dual-particle system (due to the quadrupolar interactions) is longer ( $T \geq 1$  as seen  
 278 in Fig. S2a), the two-particle globule catches up with the central particle before the  
 279 transitional reorientation can occur as observed in the dual-particle system.



280 (iii) For  $T \gtrsim 0.375$ , the three particles attach to each other to form a triple agglomerate  
 281 that moves as a whole. We note that a triplet formed of individual particles (of size  $R$ )  
 282 has an effective size of  $(1 + \sqrt{3})R \approx 0.54$  (for  $R = 0.2$ ), which is below the critical size  
 283 that maximizes the drag,  $R_{max} = 0.56$  in Fig. 5c. This results in an increased velocity  
 284 due to the enhanced drag as observed in Fig. 5c.

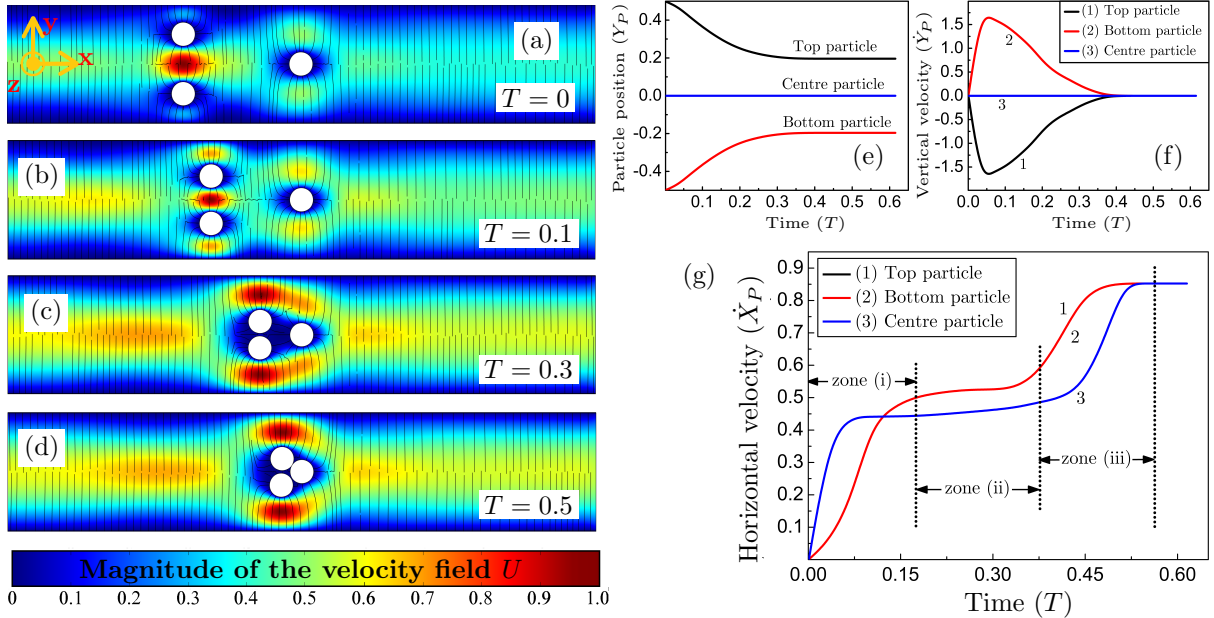
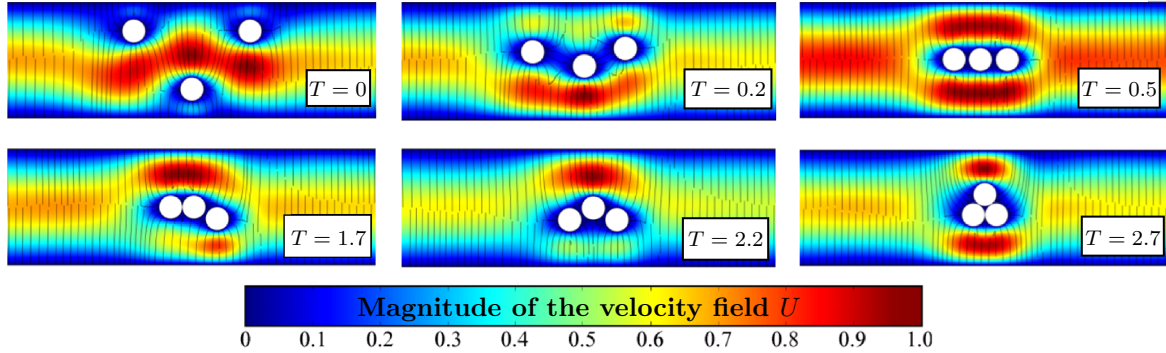


Figure 8: (a–d) Snapshots showing the evolution with time of three particles placed in a microchannel located at  $X = -0.2$ ,  $Y = \pm 0.5$  and  $X = 0$ ,  $Y = 0$ , relaxing towards the equilibrium: (a)  $T = 0$ ; (b)  $T = 0.1$ ; (c)  $T = 0.3$ ; and (d)  $T = 0.5$  (at which point the three-particle system has reached equilibrium). The fluid flow is in the positive  $x$  direction. The background colour contour represents the magnitude of the axial velocity field  $U$ . (e–g) Trajectory information of the triplet system; (e) vertical coordinates of particle centres; (f)  $Y$ -components of the particle velocities and (g)  $X$ -components of the particle velocities. Here  $R = 0.2$  and  $Er = 0.02$ . The anchoring conditions on the particle and channel walls are strongly homeotropic. All other parameters used for the calculation are given in Table 1. The boundary conditions on the particle surfaces and channel walls are homeotropic.

285 The initial configuration plays a key role in the subsequent dynamics of the triplet ag-  
 286 glomeration. For a zig-zag combination of three particles with initially large interparticle  
 287 separation distance there is an intermediate linear configuration of three particles (see  
 288 Fig. 9). The intermediate system persists for a long time ( $T = 0.5 - 2.7$ ), which suggests  
 289 that the linear state is relatively stable. The subsequent behaviour is then equivalent to  
 290 the behaviour of an initial condition of three linearly placed particles. The final configura-  
 291 tion is always found to be equiangular irrespective of the initial configuration (triangular,  
 292 zig-zag or linear) or the interparticle separation distance (see Fig. 9a, b). However, the

293 orientation of the triangular agglomerate does depend on the initial state (Figs. 8d, 9a,b).

(a) Initially (at  $T = 0$ ) the particles are located at (from left)  $(X, Y) = (-1, 0.5)$ ,  $(0, -0.5)$  and  $(1, 0.5)$



(b) Initially (at  $T = 0$ ) the particles are located at (from left)  $(X, Y) = (-0.5, 0.5)$ ,  $(0, -0.5)$  and  $(0.5, 0.5)$

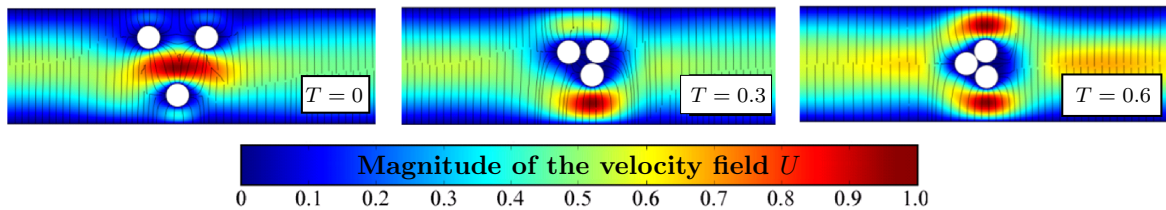


Figure 9: Snapshots showing the time evolution of the triplet arranged initially in a zig-zag configuration, for an interparticle separation distance of (a) 5 particle radii; and (b) 2.5 particle radii. Here  $R = 0.2$  and  $Er = 0.02$ . The anchoring conditions on the particle and channel walls are strongly homeotropic. All other parameter values used for the calculation are given in Table 1. The fluid flow is in the positive  $x$  direction. The background colour contour represents the magnitude of the axial velocity field  $U$ .

294 For large values of  $Er$ , the system is highly nonlinear and more topological defects are  
 295 expected. Our results are valid for  $Er < 1$ ; for  $Er > 1$ , the particle self-assembly  
 296 is influenced by the topological defects [5]. For  $Re \ll 1$  and  $Er \gtrsim 200$ , unexpected  
 297 phenomena such as cavitation around the particle has been observed [53].

## 298 4. Conclusions

299 In this paper we use a continuum Beris–Edwards framework to simulate the motion of  
 300 particles immersed in an NLC microfluidic channel, motivated by recent experimental  
 301 work. We first consider the response of the NLC director field when a particle is placed  
 302 in the channel in the absence of a flow.

303 The director orientation around the particle depends on the particle surface anchoring and  
 304 the relative particle size. The system properties also depend on the Ericksen number,  $Er$ ,  
 305 which measures the relative effect of the viscous to NLC elastic forces. As the Ericksen

306 number is increased, the hyperbolic hedgehog defect on the leading and trailing side of the  
307 particle moves further away from the particle surface, an observation that is supported  
308 by experiments [18]. The particle experiences forces due to the viscous drag and due to  
309 the interaction between the homeotropic anchored particle surfaces and channel walls. As  
310 the particle increases in size, the viscous the NLC elastic forces oppose each other and the  
311 drag force is maximum for a critical particle size. There is also a critical particle location  
312 that determines particle separation i.e. particles on either side of this critical location  
313 either migrate towards the channel walls or towards the channel centre. This gives us  
314 a potential mechanism for sorting a suspension of particles of different size, without the  
315 need for any manual separation, which is impossible in an isotropic fluid.

316 We then consider a dual-particle system, and find that the particles align at an angle of  
317 around  $39^\circ$  relative to the walls, which is close to the experimentally reported value of  
318  $41^\circ$  [48]. When a third particle is added to the system, the particles form an equiangular  
319 triplet agglomerate, in agreement with experimental observations [10]. While the final  
320 particle arrangement appears to be independent of the initial configuration, the evolution  
321 towards this final state is sensitive to the initial state, and in some instances one can obtain  
322 interim locally stable configurations. For example, a set-up of linearly aligned particles  
323 appears to be locally stable.

324 We illustrate a variety of physical phenomena that are not observed in isotropic fluids.  
325 Our numerical analysis demonstrates the rich hydrodynamic landscape for NLC microflu-  
326 idics and how the coupling between flow, anchoring, particle sizes and NLC order can be  
327 tuned to control the mechanisms of particle migration, self-reorganization and separation.  
328 We hope that our work will inspire future experimental study into particle separation and  
329 self-assembly mechanisms.

### 330 **Acknowledgements**

331 The authors gratefully acknowledge helpful discussions with L. J. Cummings and D. Vigolo.  
332 AM and IMG are grateful for discussions on nematic microfluidics with A. Sengupta and  
333 for the UK Fluids Network Short Research Visit scheme for facilitating their collabora-  
334 tion. SM is grateful to EPSRC and the Royal Society for financial support. AM's  
335 research is supported by an EPSRC Career Acceleration Fellowship EP/J001686/1 and  
336 EP/J001686/2, an OCIAM Visiting Fellowship and the Advanced Studies Centre at Ke-

337 ble College. IMG gratefully acknowledges support from the Royal Society through a  
338 University Research Fellowship.

339 **References**

- 340 [1] J. P. F. Lagerwall and G. Scalia. A new era for liquid crystal research: Applications  
341 of liquid crystals in soft matter nano-, bio-and microtechnology. *Current Applied*  
342 *Physics*, 12(6):1387–1412, 2012.
- 343 [2] A. Sengupta, U. Tkalec, M. Ravnik, J. M. Yeomans, C. Bahr, and S. Herminghaus.  
344 Liquid crystal microfluidics for tunable flow shaping. *Phys. Rev. Lett.*, 110:048303,  
345 Jan 2013.
- 346 [3] O. D. Lavrentovich. Transport of particles in liquid crystals. *Soft Matter*, 10:1264–  
347 1283, 2014.
- 348 [4] I.-H. Lin, G. M. Koenig Jr, J. J. de Pablo, and N. L. Abbott. Ordering of solid  
349 microparticles at liquid crystal–water interfaces. *J. Phys. Chem. B*, 112(51):16552–  
350 16558, 2008.
- 351 [5] A. Sengupta, C. Bahr, and S. Herminghaus. Topological microfluidics for flexible  
352 micro-cargo concepts. *Soft Matter*, 9(30):7251–7260, 2013.
- 353 [6] M. Škarabot, M. Ravnik, S. Žumer, U. Tkalec, I. Poberaj, D. Babič, N. Oster-  
354 man, and I. Muševič. Interactions of quadrupolar nematic colloids. *Phys. Rev. E*,  
355 77(3):031705, 2008.
- 356 [7] I. Muševič, M. Škarabot, U. Tkalec, M. Ravnik, and S. Žumer. Two-dimensional ne-  
357 matic colloidal crystals self-assembled by topological defects. *Science*, 313(5789):954–  
358 958, 2006.
- 359 [8] J. C. Loudet, P. Hanusse, and P. Poulin. Stokes drag on a sphere in a nematic liquid  
360 crystal. *Science*, 306(5701):1525–1525, 2004.
- 361 [9] T. Turiv, I. Lazo, A. Brodin, B. I. Lev, V. Reiffenrath, V. G. Nazarenko, and O. D.  
362 Lavrentovich. Effect of collective molecular reorientations on brownian motion of  
363 colloids in nematic liquid crystal. *Science*, 342(6164):1351–1354, 2013.
- 364 [10] P. Poulin, H. Stark, T. C. Lubensky, and D. A. Weitz. Novel colloidal interactions  
365 in anisotropic fluids. *Science*, 275(5307):1770–1773, 1997.

- 366 [11] B. Senyuk, D. Glugla, and I. I. Smalyukh. Rotational and translational diffusion  
367 of anisotropic gold nanoparticles in liquid crystals controlled by varying surface an-  
368 choring. *Physical Review E*, 88(6):062507, 2013.
- 369 [12] S. D. Peroukidis and S. H. L. Klapp. Spontaneous ordering of magnetic particles in  
370 liquid crystals: From chains to biaxial lamellae. *Phys. Rev. E*, 92:010501, Jul 2015.
- 371 [13] J.-I. Fukuda, H. Stark, M. Yoneya, and H. Yokoyama. Dynamics of a nematic liquid  
372 crystal around a spherical particle. *J. Phys.: Condensed Matter*, 16(19):S1957, 2004.
- 373 [14] O. V. Kuksenok, R. W. Ruhwandl, S. V. Shiyankovskii, and E. M. Terentjev. Di-  
374 rector structure around a colloid particle suspended in a nematic liquid crystal.  
375 *Phys. Rev. E*, 54(5):5198, 1996.
- 376 [15] R. W. Ruhwandl and E. M. Terentjev. Friction drag on a cylinder moving in a  
377 nematic liquid crystal. *Zeitschrift für Naturforschung A*, 50(11):1023–1030, 1995.
- 378 [16] S. A. Jewell, S. L. Cornford, F. Yang, P. S. Cann, and J. R. Sambles. Flow-  
379 driven transition and associated velocity profiles in a nematic liquid-crystal cell.  
380 *Phys. Rev. E*, 80(4):041706, 2009.
- 381 [17] G. Tóth, C. Denniston, and J. M. Yeomans. Hydrodynamics of topological defects  
382 in nematic liquid crystals. *Phys. Rev. Lett.*, 88(10):105504, 2002.
- 383 [18] A. Sengupta, C. Pieper, J. Enderlein, C. Bahr, and S. Herminghaus. Flow of a  
384 nematogen past a cylindrical micro-pillar. *Soft Matter*, 9(6):1937–1946, 2013.
- 385 [19] L. Giomi, L. Mahadevan, B. Chakraborty, and M. F. Hagan. Banding, excitability  
386 and chaos in active nematic suspensions. *Nonlinearity*, 25(8):2245, 2012.
- 387 [20] M. Crespo, A. Majumdar, A. M. Ramos, and I. M. Griffiths. Solution landscapes in  
388 nematic microfluidics. *Physica D: Nonlinear Phenomena*, 351:1–13, 2017.
- 389 [21] T. G. Anderson, E. Mema, L. Kondic, and L. J. Cummings. Transitions in Poiseuille  
390 flow of nematic liquid crystal. *Int. J. Non-Linear Mech.*, 75:15–21, 2015.
- 391 [22] A. Sengupta. Topological microfluidics: present and prospects. *Liquid Crystals*  
392 *Today*, 24(3):70–80, 2015.

- 393 [23] A. Sengupta. *Nematic Liquid Crystals Confined Within a Microfluidic Device: Static*  
394 *Case*, pages 72–76. Springer International Publishing, 2013.
- 395 [24] G.-Q. Chen, A. Majumdar, D. Wang, and R. Zhang. Global existence and regularity  
396 of solutions for active liquid crystals. *J. Diff. Eq.*, 263(1):202–239, 2017.
- 397 [25] D. Marenduzzo, E. Orlandini, and J. M. Yeomans. Hydrodynamics and rheology of  
398 active liquid crystals: A numerical investigation. *Phys. Rev. Lett.*, 98(11):118102,  
399 2007.
- 400 [26] A. M. Sonnet, P. L. Maffettone, and E. G. Virga. Continuum theory for nematic  
401 liquid crystals with tensorial order. *J. Non-Newtonian Fluid Mechanics*, 119(1):51–  
402 59, 2004.
- 403 [27] P. G. De Gennes. Short range order effects in the isotropic phase of nematics and  
404 cholesterics. *Molecular Crystals and Liquid Crystals*, 12(3):193–214, 1971.
- 405 [28] M. E. Cates, O. Henrich, D. Marenduzzo, and K. Stratford. Lattice Boltzmann  
406 simulations of liquid crystalline fluids: active gels and blue phases. *Soft Matter*,  
407 5(20):3791–3800, 2009.
- 408 [29] T. B. Liverpool and M. C. Marchetti. Rheology of active filament solutions.  
409 *Phys. Rev. Lett.*, 97(26):268101, 2006.
- 410 [30] A. N. Beris and B. J. Edwards. *Thermodynamics of Flowing Systems: with Internal*  
411 *Microstructure*. Oxford Engineering Science Series. Oxford University Press, 1994.
- 412 [31] J. Happel and H. Brenner. *Low Reynolds number hydrodynamics: with special ap-*  
413 *plications to particulate media*, volume 1. Springer Science & Business Media, 2012.
- 414 [32] H. Stark, D. Venzki, and M. Reichert. Recent developments in the field of colloidal  
415 dispersions in nematic liquid crystals: the stokes drag. *J. Phys.: Condensed Matter*,  
416 15(1):S191, 2002.
- 417 [33] H. Stark and D. Venzki. Stokes drag of spherical particles in a nematic environment  
418 at low Ericksen numbers. *Phys. Rev. E*, 64(3):031711, 2001.
- 419 [34] R. W. Pryor. *Multiphysics modeling using COMSOL: a first principles approach*.  
420 Jones & Bartlett Publishers, 2009.

- 421 [35] Lev Mikhaïlovich Blinov and Vladimir Chigrinov. *Electrooptic effects in liquid crystal*  
422 *materials*. Springer Science & Business Media, 2012.
- 423 [36] C. Luo, A. Majumdar, and R. Erban. Multistability in planar liquid crystal wells.  
424 *Phys. Rev. E*, 85(6):061702, 2012.
- 425 [37] T. Ikeda. Photomodulation of liquid crystal orientations for photonic applications.  
426 *J. Mater. Chem.*, 13:2037–2057, 2003.
- 427 [38] H. J. Deuling. Deformation of nematic liquid crystals in an electric field. *Molecular*  
428 *Crystals and Liquid Crystals*, 19(2):123–131, 1972.
- 429 [39] M. Schadt and W. Helfrich. Voltage-dependent optical activity of a twisted nematic  
430 liquid crystal. *Appl. Physics Lett.*, 18(4):127–128, 1971.
- 431 [40] B. Jerome. Surface effects and anchoring in liquid crystals. *Reports on Progress in*  
432 *Physics*, 54(3):391, 1991.
- 433 [41] J. Fukuda and H. Yokoyama. Stability of the director profile of a nematic liquid  
434 crystal around a spherical particle under an external field. *Eur. Phys. J. E*, 21(4):341–  
435 347, 2006.
- 436 [42] R. W. Ruhwandl and E. M. Terentjev. Monte Carlo simulation of topological defects  
437 in the nematic liquid crystal matrix around a spherical colloid particle. *Phys. Rev. E*,  
438 56(5):5561, 1997.
- 439 [43] A. Sengupta, S. Herminghaus, and B. Bahr. Liquid crystal microfluidics: surface,  
440 elastic and viscous interactions at microscales. *Liquid Crystals Reviews*, 2(2):73–110,  
441 2014.
- 442 [44] M. J. Towler, E. J. Acosta, H. G. Walton, C. Tombling, M. D. Tillin, B. Henley,  
443 E. J. Walton, T. Kawamura, A. Fujii, and Y. Yamada. Liquid crystal display device.  
444 *US Patent 6,714,276*, 2004.
- 445 [45] L. G. Leal. *Advanced transport phenomena: fluid mechanics and convective transport*  
446 *processes*. Cambridge University Press, 2007.
- 447 [46] B. H. Yang, J. Wang, D. D. Joseph, H. H. Hu, T.-W. Pan, and R. Glowinski.  
448 Migration of a sphere in tube flow. *J. Fluid Mech.*, 540:109–131, 2005.



- 449 [47] M. Tasinkevych and D. Andrienko. Colloidal particles in liquid crystal films and at  
450 interfaces. *Condensed Matter Phys.*, 13(3):1–20, 2010.
- 451 [48] F. Mondiot, R. Botet, P. Snabre, O. Mondain-Monval, and J.-C. Loudet. Col-  
452 loidal aggregation and dynamics in anisotropic fluids. *Proc. Nat. Academy Sciences*,  
453 111(16):5831–5836, 2014.
- 454 [49] B. Senyuk, O. Puls, M. Tovkach, S. B. Chernyshuk, and I. I. Smalyukh. Hexadecap-  
455 ular colloids. *Nature Comm.*, 7, 2016.
- 456 [50] M. S. Al-Barwani, G. S. Sutcliffe, and M. P. Allen. Forces between two colloidal  
457 particles in a nematic solvent. *J. Phys. Chem. B*, 108(21):6663–6666, 2004.
- 458 [51] K. Takahashi, M. Ichikawa, and Y. Kimura. Direct measurement of force be-  
459 tween colloidal particles in a nematic liquid crystal. *J. Phys.: Condensed Matter*,  
460 20(7):075106, 2008.
- 461 [52] K. Takahashi, M. Ichikawa, and Y. Kimura. Force between colloidal particles in a  
462 nematic liquid crystal studied by optical tweezers. *Phys. Rev. E*, 77(2):020703, 2008.
- 463 [53] T. Stieger, H. Agha, M. Schoen, M. G. Mazza, and A. Sengupta. Hydrodynamic  
464 cavitation in Stokes flow of anisotropic fluids. *Nature Communications*, 8, 2017.